

FE K LINE PROFILE IN LOW-REDSHIFT QUASARS: AVERAGE SHAPE AND EDDINGTON RATIO DEPENDENCE

HIROHIKO INOUE¹

Institute of Space and Astronautical Science, 3-1-1 Yoshinodai, Sagamihara, Kanagawa 229-8510, Japan

YUICHI TERASHIMA

Department of Physics, Ehime University, 2-5 Bunkyo-cho, Matsuyama, Ehime 790-8577, Japan

LUIS C. HO

The Observatories of the Carnegie Institution of Washington, 813 Santa Barbara Street, Pasadena, CA 91101-1292

Accepted for publication in the *Astrophysical Journal*

ABSTRACT

We analyze X-ray spectra of 43 Palomar-Green quasars observed with *XMM-Newton* in order to investigate their mean Fe K line profile and its dependence on physical properties. The continuum spectra of 39 objects are well reproduced by a model consisting of a power law and a blackbody modified by Galactic absorption. The spectra of the remaining four objects require an additional power-law component absorbed with a column density of $\sim 10^{23}\text{cm}^{-2}$. A feature resembling an emission line at 6.4 keV, identified with an Fe K line, is detected in 33 objects. Approximately half of the sample show an absorption feature around 0.65–0.95 keV, which is due to absorption lines and edges of O VII and O VIII. We fit the entire sample simultaneously to derive average Fe line parameters by assuming a common Fe line shape. The Fe line is relatively narrow ($\sigma = 0.36\text{keV}$), with a center energy of 6.48 keV and a mean equivalent width (EW) of 248 eV. By combining black hole masses estimated from the virial method and bolometric luminosities derived from full spectral energy distributions, we examine the dependence of the Fe K line profile on Eddington ratio. As the Eddington ratio increases, the line becomes systematically stronger (EW = 130 to 280 eV), broader ($\sigma = 0.1$ to 0.7keV), and peaks at higher energies (6.4 to 6.8 keV). This result suggests that the accretion rate onto the black hole directly influences the geometrical structure and ionization state of the accretion disk. We also examine a two-component model consisting of a Gaussian and a diskline to constrain the intensity of the broad line. The mean equivalent widths are ≈ 70 – 180eV for the four Eddington ratio groups, although the standard deviations in each group are very large. This suggests that the broad line is not ubiquitous.

Subject headings: accretion, accretion disks — galaxies: active — galaxies: nuclei — galaxies: Seyfert — quasars: general — X-rays: general

1. INTRODUCTION

Fluorescent Fe K lines are common in the X-ray spectra of accreting black holes, ranging from X-ray binaries to active galactic nuclei (AGNs), and provide one of the best probes for studying accretion disks. If the Fe K line is emitted from the inner part of the accretion disk, it becomes broad and asymmetric due to both Doppler shift and gravitational redshift (Fabian et al. 1989). The best example of a broad Fe K line is seen in the Seyfert 1 galaxy MCG-6-30-15 (Tanaka et al. 1995). Broad Fe K lines have been observed in many other sources and are thought to be very common in the X-ray spectra of Seyfert 1 nuclei (Nandra et al. 1997a).

Recent observations of AGNs with *XMM-Newton* show that the broad Fe K line is not as common as previously believed. While a few Seyfert 1 galaxies (e.g., MCG-6-30-15, Mrk 205, Mrk 509) indeed show an unambiguous broad line, Fe lines in other galaxies are dominated by a relatively narrow feature. From an analysis of 53

type 1 AGNs observed with *XMM-Newton*, Page et al. (2004a) showed that a broad Fe K line ($\sigma \geq 0.1\text{keV}$) is seen in only 13 sources, while the remaining 40 sources have a narrow line ($\sigma \leq 0.1\text{keV}$) or no lines. Some of the 13 sources show a narrow line as well as the broad line. In a similar study, Yaqoob & Padmanabhan (2004) reported the results of 18 observations of 15 Seyfert 1 galaxies observed with the *Chandra* High Energy Grating. They measured the width of the line core and obtained a weighted mean of $\text{FWHM} = 2380 \pm 760\text{ km s}^{-1}$, which is slightly larger than the instrument resolution ($\text{FWHM} \approx 1860\text{ km s}^{-1}$). Evidence of underlying broad-line emission was also found in at least four sources. Based on these recent studies, it is still controversial whether or not relativistically broadened Fe K emission is truly common in nearby AGNs.

Streblyanska et al. (2005) derived an average rest-frame spectrum of AGNs detected in a 770 ksec *XMM-Newton* observation of the Lockman Hole field. They used a sample of 104 X-ray sources with optical redshifts measured by Lehmann et al. (2001), analyzing separately the type 1 and type 2 subsamples defined by optical spectra (Schmidt et al. 1998; Lehman et al. 2001). From

Electronic address: hirohiko@astro.isas.jaxa.jp

¹ Department of Physics, Tokyo Institute of Technology, 2-12-1 Ohokayama, Meguro, Tokyo 152-8551, Japan

composite rest-frame spectra generated for the type 1 and type 2 sources, they found evidence for a broad line peaking at a rest-frame energy ~ 6.4 keV with an equivalent width (EW) ~ 560 eV and ~ 460 eV, respectively. However, it should be noted that there are some systematic uncertainties in modelling the continuum, since it is virtually impossible to distinguish a very broad line clearly from the continuum for sources as faint as those analyzed by Streblyanska et al. (2005). In addition, making composite spectra of faint sources may introduce spurious spectral features (Yaqoob 2005).

Brusa et al. (2005) and Comastri et al. (2007) studied average spectra of AGNs detected in the *Chandra* Deep Field North and South. They stacked the X-ray counts in the observed frame from spectroscopically identified AGNs, using a large number of source spectra within sufficiently narrow redshift ranges such that the energy (redshift) spread is negligible. A broad Fe line is seen in some of the stacked spectra and is fitted with a relativistic disk line model peaking at a rest-energy of 6.4 keV. Since the fluxes of the objects in the sample are low, this study may suffer from the same uncertainties affecting the Streblyanska et al. analysis of the Lockman Hole.

What parameters of the AGN affect the strength or profile of the Fe K line? An inverse correlation between the equivalent width of Fe K line and X-ray luminosity, known as the X-ray Baldwin effect, was first pointed out by Iwasawa & Taniguchi (1993). This correlation has been confirmed with *ASCA* (Nandra et al. 1997b) and *XMM-Newton* data (Page et al. 2004a; see also Jiménez-Bailón et al. 2005). The dependence of the iron line profile with luminosity was investigated by Nandra et al. (1997b) using 18 Seyfert 1s and 21 quasars observed with *ASCA*. They divided the sample into five luminosity bins and examined average Fe K line profiles. The line shows a very similar profile, which is composed of a narrow core and a broad red wing for groups with a luminosity below $L_X \approx 10^{44}$ ergs s $^{-1}$. The intensity of the narrow core, however, becomes weak above this luminosity. The red wing becomes weak and the peak energy shifts to higher energy for the luminosity range of $10^{45} \leq L_X \leq 10^{46}$ ergs s $^{-1}$; no evidence for line emission is observed above $L_X \approx 10^{46}$ ergs s $^{-1}$. Jiménez-Bailón et al. (2005), analyzing a sample of 39 Palomar-Green (PG; Schmidt & Green 1983) quasars observed with *XMM-Newton*, found a similar result as that reported by Nandra et al. (1997b). The luminosity dependence of the Fe K line may be related to the ionization level of the accretion disk.

This paper examines the behavior of the Fe K line as a function of accretion rate, as parameterized by the Eddington ratio, taking advantage of the availability of black hole mass and bolometric luminosity estimates. The Eddington ratio is a fundamental parameter that may control both the ionization state and geometric structure of the accretion disk. If so, we expect the profile of the Fe K line, in particular its width and central energy, to vary systematically with Eddington ratio. The goal of this study is to investigate this issue.

This paper is organized as follows. Section 2 describes the observations, and Section 3 shows the results of the spectral analysis of average spectra and its Eddington ratio dependence. We discuss the physical origin of the Eddington ratio dependence in Section 4. Our findings

are summarized in Section 5.

2. XMM-NEWTON OBSERVATIONS

2.1. The Sample

We selected our sample from the 87 low-redshift ($z < 0.5$) Palomar-Green quasars in Boroson & Green (1992). X-ray data for 45 objects are available in the *XMM-Newton* Science Archive (XSA). Only EPIC-PN data were used in the following analysis since the effective area of PN is much larger than that of EPIC-MOS. PG 1001+045 was excluded from the present study because no EPIC-PN data are available. PG 1226+023 (3C 273), a very bright quasar, was also excluded since it overwhelms the X-ray flux in the average spectrum examined below. Basic data (name, redshift, central black hole mass, and Eddington ratio) for the final sample of 43 objects are given in Table 1. *XMM-Newton* results of 34 objects have been published, and the references are also given in Table 1. A log of the observations is given in Table 2.

The black hole masses and Eddington ratios are taken from the study of L. C. Ho (2007, in preparation). Ho calculates black hole masses employing the virial method of Kaspi et al. (2000), using broad H β line widths from Boroson & Green (1992) and 5100 Å continuum luminosities from Neugebauer et al. (1987). His bolometric luminosities come from direct integration of the full, broad-band (radio to X-rays) spectral energy distribution rather than from a single band assuming a bolometric correction. All distance-dependent quantities were derived assuming the following cosmological parameters: $\Omega_m = 0.3$, $\Omega_\Lambda = 0.7$, and $H_0 = 72$ kms Mpc $^{-1}$. Eddington luminosities, computed assuming a composition of pure hydrogen, are given by

$$L_{\text{Edd}} = \frac{4\pi GM_{\text{BH}} m_p c}{\sigma_T} = 1.26 \times 10^{38} \left(\frac{M_{\text{BH}}}{M_\odot} \right) \text{ergs s}^{-1}, \quad (1)$$

where M_{BH} is the mass of the black hole, m_p is the proton mass, and σ_T is the Thompson scattering cross-section.

Figure 1 shows the distributions of redshift, black hole mass, and Eddington ratios. The mean redshift is $z \approx 0.2$, but the sample covers a wide range of black hole masses ($10^6 < M_{\text{BH}}/M_\odot < 10^9$) and Eddington ratios ($0.05 < L_{\text{bol}}/L_{\text{Edd}} < 4.5$).

2.2. Data Reduction

Raw data from the EPIC-PN instrument were reprocessed using Science Analysis Software (SAS) version 6.0 to produce calibrated event files. Only events with the single or double pixels (PATTERN ≤ 4) were used in the following analysis. Time intervals of background flaring were excluded. Source spectra were extracted from a circular region centered at the peak of the X-ray source counts. Background spectra were taken from an off-source region in the same field-of-view and subtracted from the source spectra. Appropriate response and ancillary files were created using the RMFGEN and ARFGEN tools in SAS, respectively. All the spectra were binned so that each bin contains at least 30 (or more for bright sources) counts in order to apply a χ^2 min-

TABLE 1
THE SAMPLE

PG	Alternate Name	z	$\log(M_{\text{BH}}/M_{\odot})$	$L_{\text{bol}}/L_{\text{Edd}}$	Group ^a	Note ^b	Reference
0003+199	Mrk 335	0.026	7.16	0.58	2		1, 2
0007+106	Mrk 1501	0.089	8.69	0.10	4	RL	3, 4
0050+124	I Zw 1	0.061	7.29	2.51	1		2, 3, 4, 5
0157+001	Mrk 1014	0.163	8.21	1.11	1		2, 3, 4
0804+761	...	0.100	8.41	0.45	2		3, 4, 5, 6
0844+349	Ton 951	0.064	7.80	0.33	3		2, 3, 4, 7, 8, 9
0947+396	...	0.206	8.67	0.26	3		2, 3, 4, 5, 10
0953+414	...	0.234	8.69	0.66	2		2, 3, 4, 5, 10
1004+130	PKS 1004+13	0.240	9.43	0.09	4	RL, BAL	11
1048+342	3C 246	0.167	8.36	0.35	3		2, 3, 4, 5, 10
1100+772	3C 249.1	0.312	9.43	0.12	4	RL	3, 4
1114+445	...	0.144	8.57	0.13	4		3, 4, 5, 10, 12
1115+407	...	0.154	7.61	1.91	1		2, 3, 4, 5, 10
1116+215	Ton 1388	0.177	8.64	0.68	2		2, 3, 4, 5, 10
1202+281	GQ Comae	0.165	8.54	0.18	3		2, 3, 4, 5, 10
1211+143	...	0.081	7.95	0.79	2		2, 3, 4, 13, 14
1216+069	...	0.331	9.40	0.18	3		3, 4, 10
1244+026	...	0.048	6.39	4.57	1		2, 3, 4, 5
1302-102	PKS 1302-102	0.27	9.04	0.48	2	RL	
1307+085	...	0.155	8.87	0.10	4		2, 3, 4, 5
1309+355	Ton 1565	0.184	8.37	0.32	3	RL	2, 3, 4, 5, 10, 12
1322+659	...	0.168	8.22	0.49	2		2, 3, 4, 5, 10
1352+183	...	0.152	8.37	0.37	3		2, 3, 4, 5, 10
1402+261	Ton 182	0.164	7.94	1.78	1		2, 3, 4, 5, 10, 15
1404+226	...	0.098	6.80	2.63	1		2, 3, 4, 16, 17
1411+442	...	0.090	7.98	0.28	3		3, 4, 10, 18
1415+451	...	0.114	7.87	0.38	3		3, 4, 10
1425+267	Ton 202	0.366	9.75	0.05	4	RL	10, 19
1426+015	Mrk 1383	0.087	8.98	0.08	4		5, 6
1427+480	...	0.221	8.10	0.71	2		2, 3, 4, 5, 10
1440+356	Mrk 478	0.079	7.42	1.91	1		2, 3, 4, 5, 10
1444+407	...	0.267	8.36	0.94	2		2, 3, 4, 10
1448+273	...	0.065	6.95	1.86	1		
1501+106	Mrk 841	0.036	8.39	0.07	4		2, 3, 4
1512+370	4C +37.43	0.371	9.50	0.13	4	RL	5, 10
1535+547	Mrk 486	0.039	7.02	0.41	3		20
1543+489	...	0.400	8.13	3.39	1		10
1613+658	Mrk 876	0.129	9.12	0.06	4		3, 4, 5, 6
1626+554	...	0.133	8.43	0.19	3		3, 4, 5, 10
2112+059	...	0.466	9.27	0.56	2	BAL	20
2130+099	Mrk 1513	0.063	7.82	0.65	2		
2214+139	Mrk 304	0.066	8.38	0.06	4		3, 4, 18
2233+134	...	0.325	8.15	2.29	1		

REFERENCES. — (1) Gondoin et al. 2002, (2) Crummy et al. 2006, (3) Piconcelli et al. 2005, (4) Jiménez-Bailón et al. 2005, (5) Porquet et al. 2004, (6) Page et al. 2004b, (7) Brinkmann et al. 2006, (8) Brinkmann et al. 2003, (9) Pounds et al. 2003, (10) Brocksopp et al. 2006, (11) Miller et al. 2006, (12) Ashton et al. 2004, (13) Pounds et al. 2003, (14) Pounds & Page 2006, (15) Reeves et al. 2004, (16) Crummy et al. 2005, (17) Dasgupta et al. 2005, (18) Brinkmann et al. 2004, (19) Miniutti & Fabian 2006, (20) Schartel et al. 2005.

^a Group divided by Eddington ratio: (1) $1.00 \leq L_{\text{bol}}/L_{\text{Edd}} \leq 2.00$, (2) $0.40 \leq L_{\text{bol}}/L_{\text{Edd}} \leq 1.00$, (3) $0.17 \leq L_{\text{bol}}/L_{\text{Edd}} \leq 0.40$, (4) $L_{\text{bol}}/L_{\text{Edd}} \leq 0.17$.

^b RL: Radio-loud quasars (Boroson & Green 1992), BAL: Broad absorption-line quasars (Weymann et al. 1991; Brandt et al. 2000).

imization technique. Spectral fits were performed with *XSPEC* version 12.2.

3. RESULTS

3.1. Spectra of Individual Objects

The spectra of most objects are not well represented by a simple power law; soft excess emission and an emission line-like feature around 6 keV are also often seen. Therefore, we considered a model consisting of a power law, a blackbody component to represent the soft excess emission below ~ 2 keV, and a Gaussian emission line around 6 keV, all modified by Galactic absorption. We used a two blackbody model for the soft excess if the single blackbody did not represent the data well. The hydrogen column densities of the Galactic absorption are left free.

Some objects show absorption features around 0.65–0.95 keV. We multiplied one or two edges to the above model for such cases.

The spectra of 39 objects are well reproduced by this model. We obtained hydrogen column densities of $N_{\text{H}} \approx (0.003-0.26) \times 10^{22} \text{ cm}^{-2}$, photon indices $\Gamma \approx 1.5$ to 2.5 , and temperatures of the blackbody $kT \approx 0.07-0.23$ keV. The column densities are consistent with the Galactic value derived from the HI map by Dickey & Lockman (1990). Except for a few cases (see Appendix), our results for individual objects are in good agreement with the independent analysis published in the references given in Table 1. The spectra of the remaining four objects (PG 1004+130, 1411+442, 1535+547, and 2214+139) show broad excess emission at energies above

TABLE 2
 OBSERVATION LOG

PG	Obs. Date	Exposure (ks)	Count rate ^a (count s ⁻¹)	$F_{2-10\text{ keV}}^{\text{b}}$ ($10^{-12}\text{ergs s}^{-1}\text{cm}^{-2}$)	$L_{2-10\text{ keV}}^{\text{c}}$ ($10^{44}\text{ergs s}^{-1}$)	Note ^d
0003+199	2000 Dec 25	28.5	19.45	13.75	0.20	1
0007+106	2000 Jul 03	10.2	3.23	7.01	1.28	
0050+124	2002 Jun 22	18.3	7.95	8.17	0.71	1
0157+001	2000 Jul 29	4.4	1.10	0.91	0.65	
0804+761	2000 Nov 04	0.5	11.22	9.94	2.45	
0844+349	2000 Nov 04	10.3	6.45	4.87	0.46	
0947+396	2001 Nov 03	17.6	1.76	1.78	2.05	
0953+414	2001 Nov 22	10.8	3.92	2.94	4.65	1
1004+130	2003 May 04	18.2	0.10	0.32	0.48	
1048+342	2002 May 13	21.5	1.17	1.30	0.94	
1100+772	2002 Nov 01	6.8	2.02	3.62	10.16	
1114+445	2002 May 14	35.0	0.53	2.28	1.12	1
1115+407	2002 May 17	14.4	2.20	1.19	0.75	
1116+215	2001 Dec 02	5.5	5.05	3.19	2.77	
1202+281	2002 May 30	12.2	2.64	3.58	2.46	1
1211+143	2001 Jun 15	48.5	3.33	3.05	0.46	2
1216+069	2002 Jul 05	5.4	0.82	1.12	3.63	
1244+026	2001 Jun 17	4.6	6.15	2.31	0.12	
1302-102	2002 Jan 03	11.5	0.61	3.05	6.44	
1307+085	2002 Jun 13	9.9	0.80	1.96	1.13	1
1309+355	2002 Jun 10	23.6	0.44	0.70	0.61	1
1322+659	2002 May 11	8.0	2.41	1.27	0.98	1
1352+183	2002 Jul 20	8.9	2.30	1.87	1.11	1
1402+261	2002 Jan 27	9.1	3.17	1.80	1.32	
1404+226	2001 Jun 18	9.1	0.59	0.13	0.03	2
1411+442	2002 Jul 10	21.6	0.12	0.46	0.08	1
1415+451	2002 Dec 08	20.4	1.43	1.06	0.34	
1425+267	2002 Jul 28	29.6	0.67	1.68	6.29	1
1426+015	2000 Jul 28	2.2	9.39	8.48	1.50	
1427+480	2002 May 31	32.5	1.15	1.05	1.44	
1440+356	2003 Jan 04	10.8	5.58	2.63	0.39	
1444+407	2002 Aug 11	16.7	0.96	0.45	1.05	
1448+273	2003 Feb 08	18.0	4.23	2.07	0.20	
1501+106	2001 Jan 13	7.6	18.31	15.00	0.44	1
1512+370	2002 Aug 25	15.4	1.54	1.87	7.98	1
1535+547	2002 Nov 03	14.4	0.16	1.33	0.04	
1543+489	2003 Feb 08	3.7	0.35	0.13	0.87	
1613+658	2001 Aug 29	2.4	4.46	4.98	2.05	1
1626+554	2002 May 05	4.8	2.84	2.86	1.28	
2112+059	2003 May 14	7.4	0.13	0.34	2.24	
2130+099	2003 May 16	23.3	2.13	3.63	0.32	1
2214+139	2002 May 12	6.2	0.55	3.32	0.31	1
2233+134	2003 May 28	6.2	0.59	0.49	1.69	1

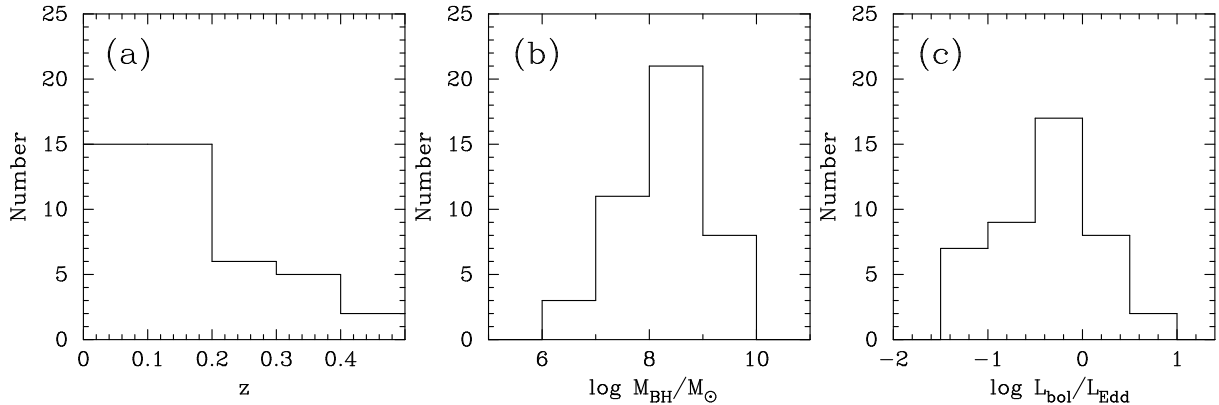
^a Count rate in 0.3–15 keV.^b Flux in 2–10 keV, not corrected for absorption.^c Luminosity in 2–10 keV, not corrected for absorption.^d Signature of ionized absorber. 1: one edge; 2: two edges.

FIG. 1.— Distribution of (a) redshifts, (b) central black hole masses, and (c) Eddington ratios.

$\sim 2\text{--}3$ keV. We added an absorbed power-law component to the model used above to represent this component. This model provides a good description of the spectra. The hydrogen column densities of the absorbed power law are $\sim 10^{23} \text{ cm}^{-2}$ for all the cases. Details of the spectral fits to these four quasars are given in Appendix A. The spectral parameters for the other components are similar to those obtained for the 39 objects without an additional absorbed power law.

An absorption feature around 0.65–0.95 keV, which can be well fitted by one or two edges, is seen in 20 out of the 43 objects. The majority of the sources (18/20) require only a single edge, with a mean edge energy of $E = 0.69$ keV and an optical depth of $\tau = 0.56$. The absorption features in the two remaining objects are represented by two edges: for PG 1211+143, the edge energies are $E = 0.75^{+0.02}_{-0.01}/0.93^{+0.02}_{-0.01}$ keV and the optical depths are $\tau = 0.36^{+0.05}_{-0.05}/0.31^{+0.04}_{-0.07}$; for PG 1404+226, the parameters are $E = 0.74^{+0.12}_{-0.06}/0.94^{+0.04}_{-0.03}$ keV and $\tau = 0.25^{+0.22}_{-0.21}/0.89^{+0.38}_{-0.37}$. Similar features are often seen in Seyfert 1s and quasars observed with the energy resolution of CCD. High-resolution spectroscopy of such features with grating spectrometers onboard *XMM-Newton* and *Chandra* have shown that they consist of many absorption lines of ionized species such as He-like and hydrogenic O, Ne, and Mg. The observed edge energies are in agreement with such ionized absorbers observed with CCD resolution (e.g., George et al. 1998, 2000).

The fluxes and luminosities obtained for the best-fit model, as well as the detected count rates, are summarized in Table 2. Neither the fluxes nor the luminosities are corrected for absorption.

3.2. Co-added Spectra

We derived a co-added rest-frame spectrum of the 43 quasars in order to examine the average shape of the Fe K emission line. Since each object has a different redshift and thus a different observed line energy, the detector response, which is energy dependent, is different for each object. As the co-added rest-frame spectrum is a summation of spectra taken with different energy resolution, this situation complicates quantitative analysis. Therefore, the spectrum derived here is for presentation purpose only, and quantitative analysis by simultaneous fitting is done in the next subsection.

The co-added spectrum was constructed as follows. First, ratios of the data to the best-fit continuum model were calculated. The ratios were then multiplied by the unfolded best-fit continuum model. The resulting spectrum is composed of an unfolded continuum and a folded emission-line component. The energy scales of both the unfolded continuum spectrum and the spectrum consisting of the unfolded continuum plus the folded line were shifted to the source redshift. We selected bin widths of 0.25 keV for $E \leq 8$ keV and 2.5 keV for $E \geq 8$ keV in this process, and used a Monte Carlo method to redistribute the observed events into the new spectral bins. The 43 spectra with the folded line are then co-added. The unfolded continuum model spectra were also co-added. Finally, the ratio of the two spectra is calculated, as shown in Figure 2. A prominent narrow core at ~ 6.4 keV and a very weak low-energy wing are seen.

3.3. Simultaneous Fit to All Spectra

In contrast to previous studies, we employ simultaneous fits rather than fits to stacked spectra. Since the Fe K line in each quasar has a different peak energy in the observed frame according to their redshifts, a technique that properly treats the energy-dependent detector response is necessary. We fitted all spectra simultaneously in order to determine mean Fe K line parameters. The spectral parameters of the best-fit continuum models for each object were used as initial parameters in the spectral fits. All the continuum parameters were left free, while the parameters for the edge model are fixed at the best-fit values for individual fits. A Gaussian model with common peak energy and width is added to the continuum model. The normalizations of the Gaussian component were left free individually. The fitting results are shown in Table 3. The best-fit peak energy and the dispersion of the Gaussian line are $E = 6.48^{+0.05}_{-0.04}$ keV and $\sigma = 0.36^{+0.08}_{-0.08}$ keV, respectively. The mean of the distribution of the equivalent widths, shown in Figure 3, is 248 eV, with a standard deviation of 168 eV.

A relativistic line model (`diskline` model in XSPEC) instead of a Gaussian was also examined. We fixed several parameters; the peak energy at 6.4 keV, the outer radius R_{out} at $500 R_s$, where R_s is the Schwarzschild radius, the emissivity index β at -2, and the inclination angle of the disk i at 30 degrees. The free parameters are the inner radius R_{in} and the intensity of the line. Again, the parameters in the continuum model were initially set to the best-fit values in the individual fits and left free except for the edge component. The results are summarized in Table 3. The best-fit inner radius R_{in} is $3.0^{+3.3}_{-0.0} R_s$. The lower boundary is fixed at $3R_s$, which is the minimum value allowed in the `diskline` model assuming a Schwarzschild black hole. The mean and standard deviation of the equivalent widths are 210 eV and 133 eV, respectively.

The line profile in Figure 2 shows a prominent narrow core and a very weak low-energy wing. Such a profile may be indicative of the presence of multiple line components, and a single Gaussian or a diskline profile may not be a good representation. Therefore, we examined a two-component line model consisting of either two Gaussians or a combination of a Gaussian and a diskline component. With regards to the double-Gaussian model, although the χ^2 improved by 103 for 3 additional parameters, not all the line parameters were tightly constrained. Thus, we first fixed the continuum component to obtain a rough value of the Gaussian widths, and then the widths were fixed at these values to constrain the equivalent widths of the lines. All the parameters except for the widths were left free in the latter fit. Note that the normalizations of the lines were determined for each object. The resulting peak energies of the broad and narrow lines are 5.06 keV and 6.52 keV, respectively (see Table 3). The mean equivalent width for the narrow component is 261 eV, and for the broad component it is 150 eV, although the standard deviations of the distributions are large (171 and 181 eV, respectively). The distributions suggest that the narrow component is commonly seen and that the broad line is present in a fraction of the sample.

The Gaussian plus diskline model was then examined. We fixed the peak energy and the dispersion of the Gaus-

sian to the best-fit parameters of the narrow component in the double-Gaussian fit. The fixed parameters for the diskline component were the same as those in the single diskline fit presented above. The free parameters are the inner radius and the normalization of the diskline, and the parameters for the Gaussian and continuum. As summarized in Table 3, the best-fit inner radius is $R_{\text{in}} = 3.0^{+5.9}_{-0.0} R_{\text{S}}$, and the mean equivalent width of the diskline is $\text{EW} = 102 \text{ eV}$. The large standard deviation (181 eV) again suggests that the diskline is required in only a fraction of the sample.

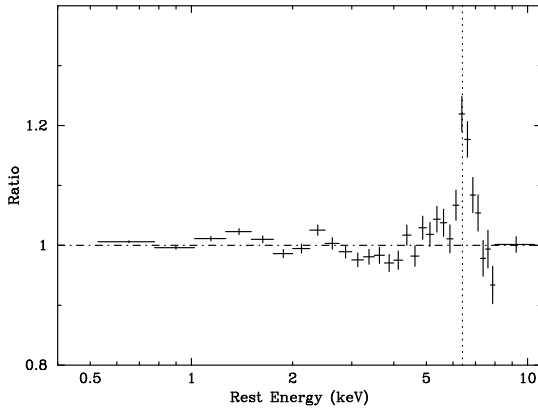


FIG. 2.— Data-to-model ratio for co-added spectrum of 43 PG quasars. Vertical dotted line is at 6.4 keV.

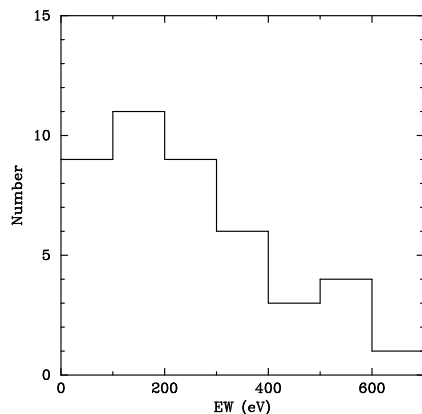


FIG. 3.— Distribution of equivalent widths of Fe K line in 43 PG quasars. A single Gaussian model is assumed.

3.4. Eddington Ratio Dependence of the Fe Line Profile

We now turn to the Eddington ratio dependence of the Fe line profile. The 43 quasars were divided into four groups according to the Eddington ratio as follows: (1) $1.00 \leq L_{\text{bol}}/L_{\text{Edd}}$, (2) $0.40 \leq L_{\text{bol}}/L_{\text{Edd}} \leq 1.00$, (3) $0.18 \leq L_{\text{bol}}/L_{\text{Edd}} \leq 0.40$, and (4) $L_{\text{bol}}/L_{\text{Edd}} \leq 0.18$ (see Table 1). The spectra in each group were co-added as in Section 3.3 for the purposes of presentation; Figure 4 shows the resulting data-to-continuum model ratios. As the Eddington ratio increases, the width of the Fe K line appear to becomes broader and its peak energy rises.

Following the procedure outlined in Section 3.3, we fitted the spectra in each group simultaneously to characterize the Fe K line quantitatively. The following four

models were examined for the Fe K line component: single Gaussian, single diskline, double Gaussians, and a Gaussian plus diskline model. The results of the spectral fits are shown in Table 4, and the Eddington ratio dependence of the peak energy and the width of the line obtained from the single Gaussian model fits are shown in Figure 5. We again find that the width and peak energy of the line become broader and higher as the Eddington ratio increases. The peak energy gradually increases from 6.37 keV in group 4 to 6.77 keV in group 1. The width is relatively narrow ($\sigma = 0.15 \text{ keV}$) in group 4, but definitely resolved ($\sigma_{\text{inst}} = 0.07 \text{ keV}$), and becomes wider ($\sigma = 0.68 \text{ keV}$ in group 1) as $L_{\text{bol}}/L_{\text{Edd}}$ increases. The distributions of the equivalent widths for each group obtained from the Gaussian fits are shown in Figure 6; the mean equivalent widths in each group are 280, 276, 287, and 131 eV, respectively.

A diskline model was examined next. We fixed several diskline parameters. The line center energy was chosen to be 6.4 keV for groups 3 and 4 and 6.7 keV for groups 1 and 2, for which the Gaussian fits suggest that the line is from ionized Fe. The outer radius R_{out} , the emissivity index β , and the inclination angle i were fixed at $500 R_{\text{S}}$, -2 , and 30 degrees, respectively. The free parameters are the inner radius R_{in} and the normalization. The parameters for the continuum model were also left free, except for those of the edge component. The results are shown in Table 4. The resulting values of χ^2 are similar to or slightly worse than those for the Gaussian fits. The best-fit inner radius is $R_{\text{in}} \approx 3R_{\text{S}}$, which is the last stable orbit of a Schwarzschild black hole.

We also examined a two-component line model since a strong narrow core and a broad wing are visible in groups 3 and 4, and possibly in group 2. A double-Gaussian model was first tested in the same way as in Section 3.3; the results are shown in Table 4. The resulting χ^2 values are similar to or only slightly better than those of the single-Gaussian fit, indicating that the additional broad line is statistically not required. The distributions of the EW are broad and indicate that some objects may have a broad component.

A Gaussian plus diskline model was then used in order to constrain the equivalent width of the diskline, in which the inner radius is fixed at $3R_{\text{S}}$. The peak energy and the dispersion of the Gaussian were fixed at the best-fit parameters for the narrow component in the double-Gaussian fit. The inner radius of the disk was also fixed at $3R_{\text{S}}$, and the other parameters in the diskline model were fixed to the same values as in the single-diskline fits described above. Only the normalizations of the Gaussian and diskline were left free. The parameters for the continuum model were treated in a similar way as in Section 3.3. The results are summarized in Table 4. The resulting values of χ^2 are similar to or only slightly better than those for the single-Gaussian or diskline fits. The mean equivalent widths of the diskline in each group are 99, 176, 132, and 67 eV, respectively, although the standard deviations as large. The large standard deviations again suggest that the broad diskline is not ubiquitous.

4. DISCUSSION

4.1. Origin of the Eddington Ratio Dependence

We examined mean Fe K line shapes for the four groups sorted by the Eddington ratios, and found that the peak

TABLE 3
RESULTS OF SPECTRAL FIT.

Model	Gaussian			Diskline						$\chi^2/\text{d.o.f.}$
	Energy (keV)	σ (keV)	EW ^a (eV)	Energy (keV)	R_{in} (R_s)	R_{out} (R_s)	β	i (deg)	EW ^a (eV)	
Gaussian	$6.48^{+0.05}_{-0.04}$	$0.36^{+0.08}_{-0.08}$	248(168)	—	—	—	—	—	—	8958/8129
Diskline	—	—	—	6.4f	$3.0^{+3.3}_{-0.0p}$	500f	—2f	30f	210(133)	8975/8130
Gaussian+Gaussian	$5.06^{+0.17}_{-0.13}$	0.61f	150(181)	—	—	—	—	—	—	—
	$6.52^{+0.05}_{-0.04}$	0.34f	261(171)	—	—	—	—	—	—	8853/8086
Gaussian+Diskline	6.52f	0.34f	155(181)	6.4f	$3.0^{+2.9}_{-0.0p}$	500f	—2f	30f	102(122)	8912/8087

^aNumbers in parentheses are standard deviation of distribution of best-fit values.

^b“p” denotes pegged parameter.

^c“f” denotes fixed parameter.

TABLE 4
RESULTS OF SPECTRAL FIT IN EACH EDDINGTON RATIO GROUP.

Group	Model	Gaussian			Diskline						$\chi^2/\text{d.o.f.}$
		Energy (keV)	σ (keV)	EW ^a (eV)	Energy (keV)	R_{in} (R_s)	R_{out} (R_s)	β	i (deg)	EW ^a (eV)	
1	Gaussian	$6.77^{+0.30}_{-0.30}$	$0.68^{+0.38}_{-0.24}$	280(199)	—	—	—	—	—	—	2308/2237
	Diskline	—	—	—	6.7f	$3.0^{+20.0}_{-0.0p}$	500f	—2f	30f	202(176)	2316/2238
	Gaussian+Gaussian	$6.58^{+0.14}_{-0.56}$	0.42f	119(152)	—	—	—	—	—	—	—
		$7.47^{+0.58}_{-1.44}$	0.48f	257(395)	—	—	—	—	—	—	2305/2248
2	Gaussian+Diskline	7.47f	0.48f	208(281)	6.7f	3.0f	500f	—2f	30f	99(158)	2304/2250
	Gaussian	$6.54^{+0.08}_{-0.08}$	$0.35^{+0.14}_{-0.07}$	276(160)	—	—	—	—	—	—	2636/2197
	Diskline	—	—	—	6.7f	$3.0^{+1.9}_{-0.0p}$	500f	—2f	30f	285(171)	2662/2198
	Gaussian+Gaussian	$5.02^{+0.30}_{-0.25}$	0.38f	90(137)	—	—	—	—	—	—	—
3		$6.52^{+0.07}_{-0.07}$	0.24f	183(96)	—	—	—	—	—	—	2634/2218
	Gaussian+Diskline	6.52f	0.24f	68(80)	6.7f	3.0f	500f	—2f	30f	176(203)	2646/2220
	Gaussian	$6.45^{+0.09}_{-0.10}$	$0.37^{+0.25}_{-0.12}$	287(179)	—	—	—	—	—	—	1796/1774
	Diskline	—	—	—	6.4f	$3.3^{+8.0}_{-0.3p}$	500f	—2f	30f	259(149)	1801/1775
4	Gaussian+Gaussian	$5.55^{+0.46}_{-0.87}$	0.48f	96(123)	—	—	—	—	—	—	—
		$6.49^{+0.09}_{-0.08}$	0.25f	173(124)	—	—	—	—	—	—	1800/1798
	Gaussian+Diskline	6.49f	0.25f	83(114)	6.4f	3.0f	500f	—2f	30f	132 (132)	1803/1800
	Gaussian	$6.37^{+0.05}_{-0.04}$	$0.15^{+0.06}_{-0.02}$	131(59)	—	—	—	—	—	—	2184/1935
4	Diskline	—	—	—	6.4f	$3.0^{+24.2}_{-0.0p}$	500f	—2f	30f	179(68)	2186/1936
	Gaussian+Gaussian	$5.90^{+0.37}_{-0.56}$	0.70f	104(108)	—	—	—	—	—	—	—
		$6.37^{+0.04}_{-0.03}$	0.09f	82 (70)	—	—	—	—	—	—	2173/1957
	Gaussian+Diskline	6.37f	0.09f	75(76)	6.4f	3.0f	500f	—2f	30f	67(73)	2180/1959

^aNumbers in parentheses are standard deviation of distribution of best-fit values.

^b“p” denotes pegged parameter.

^c“f” denotes fixed parameter.

energy, width, and equivalent width become higher (6.4 to 6.8 keV), broader (0.1 to 0.7 keV), and larger (130 to 280 eV), respectively, as the Eddington ratio increases. In this section, we discuss possible reasons of the observed Eddington ratio dependence of the Fe line profile.

The line center energy of the Fe K line is governed by a combination of the Doppler effect caused by the orbital motion, gravitational redshift, and the ionization state of the emitter. An Fe line from a rotating disk around a black hole shows a double-peaked profile with a peak energy that depends on the inclination angle of the disk. Since each of the four groups we used contains from 10 to 11 objects, it is unlikely that any one of the groups has a mean inclination angle considerably different from those of other groups. Therefore, the different line center energies obtained for the four groups probably reflect different ionization states rather than different mean disk inclination angles. The Eddington ratio dependence of

the peak energy thus strongly suggests that the ionization state of the accretion disk depends on the Eddington ratio. Many aspects of an ionized disk have been studied theoretically over the last decade. Calculations have been performed for constant-density atmospheres (e.g., Matt et al. 1993; Ross & Fabian 1993; Źycki et al. 1994), as well as for atmospheres in hydrostatic equilibrium (Nayakshin et al. 2000; Ballantyne et al. 2001). These authors calculated reflection spectra from an ionized disk for different conditions. In the lowest ionization regime, the most prominent feature is the cold iron line at 6.4 keV. As the mass accretion rate goes up, the ionized stage becomes higher, and the Fe K line is dominated by Fe XXV and XXVI, and K lines from the lighter elements emerge in the 0.3 – 3 keV band. At very high accretion rates, the surface of the disk is highly ionized so that the only noticeable line is a Compton-broadened Fe K line peaking at \sim 7 keV. The Eddington ratio dependence of

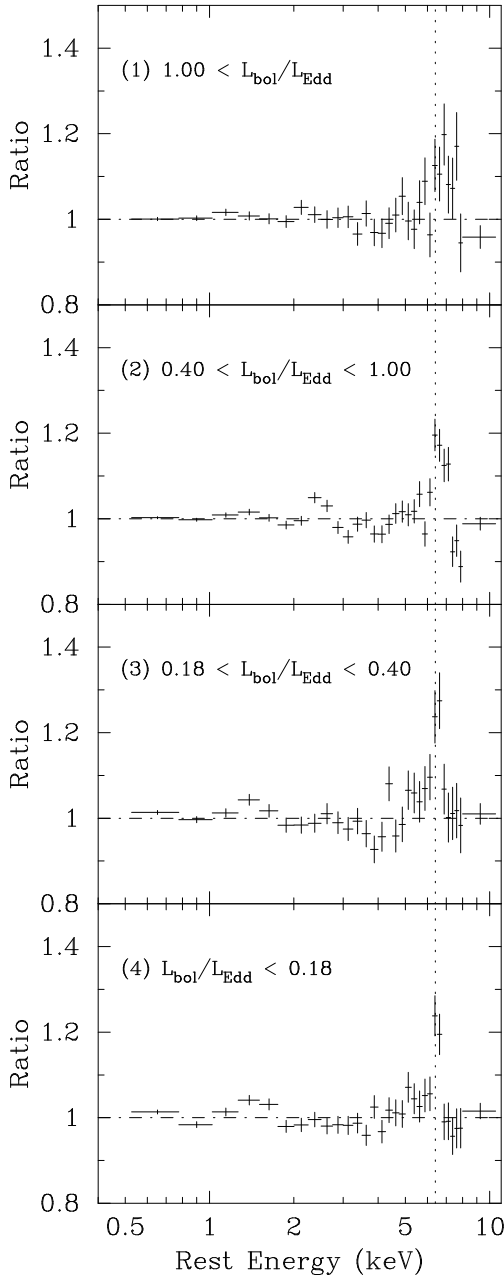


FIG. 4.— Eddington ratio dependence of the Fe line profile for each of the four groups. The vertical dotted line is at 6.4 keV.

the peak energy and the width of the Fe K line we observed in the PG quasar sample is in good agreement with the predictions of ionized disk models.

The large EW in the high-Eddington ratio groups is also likely to be related to the ionization state of the accretion disk. Calculations of the reflected X-rays from an ionized disk have shown that the EW of the Fe K line can be higher than in the case of a disk in a low-ionization state. The resonant trapping effect plays a role in the intermediate-ionization state higher than Fe XVIII. The EW increases again from Fe XX, reaching a maximum value of 250 – 300 eV (Matt et al. 1993; Ross & Fabian 1993; Źycki & Czerny 1994). The observed line center energies and EWs for the three groups with a largest Eddington ratios are consistent with the latter expectation,

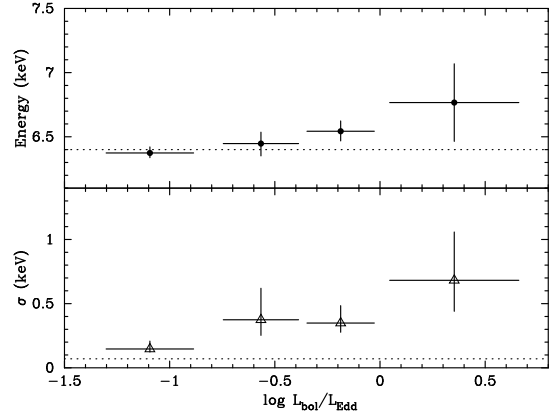


FIG. 5.— Eddington ratio dependence of the peak energy and the width of the line. The horizontal dotted line on the top panel is at 6.4 keV, and that on the bottom panel is at 0.07 keV, the instrumental resolution of *XMM-Newton*.

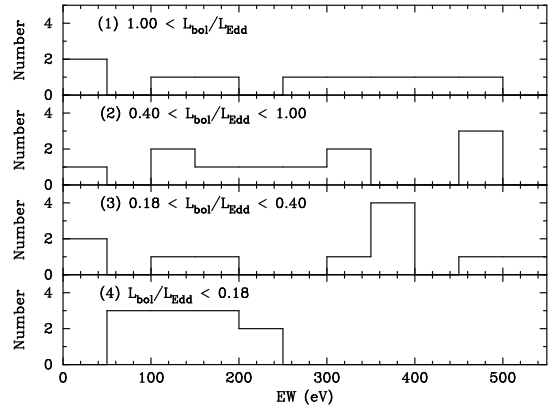


FIG. 6.— Distribution of Fe line equivalent width in each Eddington ratio group.

although the scatter of the actual EW distributions is large. The reduction of EW caused by resonant trapping is not clearly seen in our data. This may be due to the coarse binning of the Eddington ratio we have adopted. Future analysis of a larger sample may be able to see the ionized disk in an intermediate-ionization state.

The Eddington ratio dependence of the line width also suggests a change of the geometrical structure of the disk, if the velocity width indeed reflects emission from the inner part of an accretion disk broadened by Doppler effects and gravitational redshift. Although the line widths obtained from the single-Gaussian fits are consistent with systematic variations in the inner disk radius R_{in} , such a trend is not clear in the fits obtained using the diskline model. It is possible that the broader line widths at high Eddington ratios may in part be accounted for by a blend of lines from Fe in different ionization states.

4.2. Comparison with Average Fe Line Profile of AGNs in Lockman Hole

Streblyanska et al. (2005) derived an average Fe line profile of 53 type 1 AGN detected in a 770 ks observation of the Lockman Hole with *XMM-Newton*. Their average spectrum shows a broad line-like feature ($\sigma = 0.69$ keV) peaking at 6.4 keV with an equivalent width of $\text{EW} = 420$ eV. The profile is asymmetric, with a significant wing

seen toward low energies. The line width ($\sigma = 0.36$ keV) we obtained for the PG quasar sample is significantly narrower, and the equivalent width ($EW \approx 250$ eV) smaller, than that of Streblyanska et al.'s profile. We discuss possible causes for the difference.

4.2.1. Contribution of Absorbed Quasars

Appropriate modeling of the continuum is essential to derive a correct Fe line profile. A single power-law model was assumed in the analysis of the AGNs in the Lockman Hole. Since the spectra of many AGNs show a signature of absorption by ionized and/or cold matter, a simple power law may not be a good approximation of the underlying continuum. Indeed, four quasars in our sample are absorbed by a large column density ($N_H \approx 10^{23}$ cm $^{-2}$). If there are some highly absorbed objects in the Lockman Hole sample, using a single power-law model for the continuum may mimic a broad-line profile.

The flux of a highly absorbed power law with a column density of 10^{23} cm $^{-2}$ at 5 keV is about 50% of that of an unabsorbed power law. If the fraction of highly absorbed quasars is 1/10, their contribution to the low-energy side of the Fe K line profile around 5 keV is less than 5%. The contribution of the absorbed continuum depends on the fraction of absorbed quasars. Mateos et al. (2005) measured the absorbed fraction for their sample of Lockman Hole AGNs with sufficient X-ray counts. They found that seven out of 46 type 1 AGNs show a highly absorbed spectrum. This fraction is similar to that in our PG quasar sample. Note, however, that Streblyanska et al.'s sample may contain more highly absorbed objects because their flux limit is lower than that used by Mateos et al. (2005) and X-ray surveys have shown that objects with lower flux tend to have a harder spectrum. If the absorbed fraction is 10% or higher, rather than 5%, in the Lockman hole sample, a considerable fraction of the red wing might be explained by the contribution of highly absorbed emission.

4.2.2. Distribution of Luminosities

The physical state of an accretion disk may depend on luminosity. If the mean luminosity of our sample is fairly different from that of the Lockman Hole AGNs, it may introduce a difference in the Fe K line profile. In order to examine this possibility, we compared the distributions of the 2 – 10 keV luminosity between the two samples (Fig. 7). The luminosities of the Lockman Hole AGNs were taken from Mainieri et al. (2002). They analyzed 39 type 1 AGNs in the *XMM-Newton* observation of the Lockman Hole field. Most of the 53 type 1 AGNs in Streblyanska et al. (2005) have been analyzed by Mainieri et al. (2002). The two distributions are very similar, and their mean luminosities are essentially identical: the mean luminosity of our sample is $10^{43.98}$ ergs s $^{-1}$, while that of the Lockman Hole AGNs is $10^{44.00}$ ergs s $^{-1}$. We conclude that luminosity differences is not the main cause of the difference of the line profiles.

4.2.3. Artificial Distortion of Spectra

Yaqoob (2005) pointed out a spurious effect in adding spectra of faint sources. He showed that conventional methods for averaging low signal-to-noise ratio X-ray spectra result in a weakening of emission lines, a broad

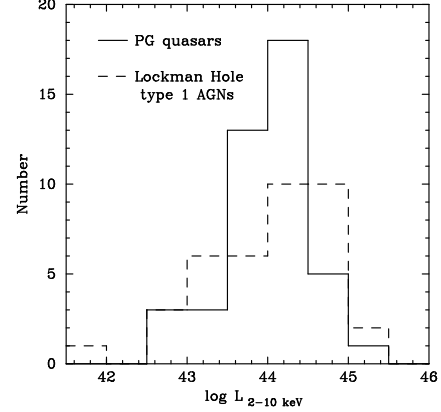


FIG. 7.— Distribution of luminosities for the PG quasars in our sample and for the AGNs in the Lockman Hole. Mean luminosities are $L_{PG}=10^{43.98}$ ergs s $^{-1}$ and $L_{LH}=10^{44.00}$ ergs s $^{-1}$, respectively.

dip in the continuum above an emission line, and a spectral hardening at the highest energies, if sources at different redshifts are stacked. Yaqoob (2005) simulated 200 spectra from sources with redshifts 0.5–2.5 and 2–10 keV fluxes $6\text{--}60 \times 10^{-14}$ ergs cm $^{-2}$ s $^{-1}$ and found an artifact wing at energies below the peak of the Fe K line. This feature occurs at the level of about 5%–10% at 4–6 keV. This kind of spectral distortion may affect the Fe line shape in the analysis of Streblyanska et al. (2005) since their sample has a relatively low average flux ($F_{2-10\text{ keV}} \approx 10^{-14.0}$ ergs s $^{-1}$ cm $^{-2}$), compared to our PG quasar sample ($F_{2-10\text{ keV}} \approx 10^{-11.5}$ ergs s $^{-1}$ cm $^{-2}$).

5. CONCLUSIONS

We presented the average Fe K line profile of 43 PG quasars observed by *XMM-Newton*. Our findings are summarized as follows.

- The spectra of 39 objects are well reproduced by a canonical model consisting of a power law, a blackbody, an edge in the case of objects with evidence for warm absorption, and a Gaussian, all modified by Galactic absorption, while that of the remaining four objects require additional absorption with a column density of 10^{23} cm $^{-2}$ to the power-law component.
- An average spectrum of the 43 quasars shows a prominent narrow Fe K line ($E = 6.48$ keV, $\sigma = 0.36$ keV, and $EW = 248$ eV).
- The average Fe K line is well represented by double Gaussians or a combination of a Gaussian and a diskline model. The best-fit inner radius of the disk is $3R_S$ ($\leq 5.9R_S$) and the mean EW is ~ 100 eV. The large standard deviation of the EW distribution indicates that a broad disklike line is not ubiquitous.
- We found an Eddington ratio dependence of the Fe K line profile. As the Eddington ratio increases, the peak energy becomes higher (6.4 to 6.8 keV), the width becomes broader (0.1 to 0.7 keV), and the EW is larger (130 to 280 eV). The higher energy peak and larger EW at high Eddington ratio can be explained by the ionization of the accretion

TABLE 5
SPECTRAL PARAMETERS FOR HIGHLY ABSORBED QUASARS.

PG	Γ	kT (keV)	$(N_{\text{H}})_{z=0}^{\text{a}}$ (10^{22} cm^{-2})	N_{H}^{b} (10^{22} cm^{-2})	Edge/ τ (keV)	E_{Fe} (keV)	σ (keV)	EW (eV)	$\chi^2/\text{d.o.f.}$
1004+130	$1.93^{+0.30}_{-0.36}$	—	$0.06^{+0.03}_{-0.03}$	$5.04^{+2.56}_{-1.69}$	—	—	—	—	20/14
1411+442	$1.55^{+0.24}_{-0.23}$	$0.13^{+0.01}_{-0.01}$	$0.03^{+0.05}_{-0.03}$	$16.7^{+4.5}_{-5.6}$	$0.72^{+0.02}_{-0.03}/0.85^{+0.35}_{-0.35}$	$6.35^{+0.14}_{-0.34}$	$0.25^{+0.60}_{-0.17}$	481^{+3249}_{-481}	63/75
1535+547	$2.24^{+0.28}_{-0.16}$	$0.07^{+0.03}_{-0.01}$	$0.27^{+0.14}_{-0.07}$	$11.9^{+1.9}_{-2.1}$	$0.93^{+0.15}_{-0.20}/1.86^{+1.89}_{-1.50}$	6.4f	$0.00 (< 0.24)$	81^{+262}_{-81}	91/87
2214+139	$1.49^{+0.15}_{-0.14}$	$0.18^{+0.02}_{-0.07}$	$0.02^{+0.12}_{-0.02}$	$2.4^{+1.24}_{-0.21}$	$0.73^{+0.02}_{-0.03}/1.13^{+0.44}_{-0.42}$	6.4f	$0.06^{+0.15}_{-0.06}$	152^{+484}_{-152}	146/106

^a Foreground absorption within our Galaxy

^b Absorption within quasar

disk. The systematic broadening of the line with increasing Eddington ratio may indicate a systematic decrease of the inner radius of the disk, or perhaps blending from a combination of Fe lines in different ionization states.

- The line width we obtained is narrower and the equivalent width smaller than those derived from

the stacked spectrum of AGNs in the Lockman Hole ($\sigma = 0.69$ keV, EW = 420 eV). We attribute these differences to either an increased contribution of absorbed sources in the Lockman Hole composite spectrum or to artifacts introduced in averaging faint sources.

APPENDIX

NOTES ON INDIVIDUAL OBJECTS

Highly Absorbed Quasars

We found four highly absorbed quasars in the 43 PG quasars. We show their spectra in Figure 8. They are not well reproduced by the canonical model, and an additional highly absorbed component is required. Therefore, we added an absorbed power-law component. The fitting results are summarized in Table 5. The average column densities of the additional absorption are $\sim 10^{23} \text{ cm}^{-2}$. Spectra of PG 1411+442 and PG 2214+139 are presented in Brinkmann et al. (2004). The results of PG 1411+442 are consistent with ours. The reduced χ^2 value is not good for PG 2214+139 ($\chi^2_{\nu} \approx 1.38$) because of non-systematic deviations of the data from the model seen over the energy range of 0.5–4 keV. Miller et al. (2006) and Schartel et al. (2005) found absorbed emission in PG 1004+130 and PG 1535+547, respectively. The results obtained by Miller et al. (2006) are also consistent with ours. Schartel et al. (2005) found the peak energy of Fe K line at $6.00^{+0.14}_{-0.21}$ keV and the width of $0.26^{+0.21}_{-0.11}$ keV, while the line center energy is lower than 5 keV in our analysis. Therefore, we fixed it at 6.4 keV and repeated the fits. The best-fit line width is $\sigma = 0.00 (< 0.24)$ keV (see Table 5).

A population of soft X-ray-weak (SXW) quasars, where the soft X-ray flux is $\sim 10 - 30$ times smaller than in typical quasars (Yuan et al. 1998), has been known. This class comprises $\sim 10\%$ of optically selected quasars. Brandt et al. (2000) found 10 SXW quasars in the Boroson & Green (1992) sample of 87 PG quasars. All of the highly absorbed quasars presented here are consistent with the SXW classification of Brandt et al. (2000). The large absorption seems to be the cause of the X-ray weakness at least in these four objects.

Quasars Newly Analyzed in This Paper

We summarize the results of our spectral analysis of quasars newly presented in this paper. Their spectra are shown in Figure 9. We fitted the spectra with the canonical model described in Section 3.1; results are listed in Table 6. They are well reproduced by the model except for one case (PG 1448+273). The soft excess component in PG 1448+273 is not explained by a single blackbody component. We added an additional blackbody component and obtained a good fit.

Quasars Reanalyzed in This Paper

This section shows results of quasars reanalyzed in this paper, for which the best-fit parameters are not consistent with previously published results. Our results are summarized in Table 7. Some notes on individual objects are given below.

PG 0003+199.— Gondoin et al. (2002) give the line center of Fe K line at 6.0 ± 0.14 keV and the width of 1.2 ± 0.2 keV. We obtained a higher center energy $6.60^{+0.13}_{-0.02}$ keV and a narrower width $0.35^{+0.16}_{-0.09}$ keV.

PG 0804+761.— Jiménez-Bailón et al. (2005), Porquet et al. (2004), and Page et al. (2004) show the best-fit parameters of the line center at 6.38 ± 0.06 , $6.67^{+0.31}_{-0.37}$, and 6.62 ± 0.14 keV, respectively. The peak energy measured by Porquet et al. (2004) and Page et al. (2004b) are consistent with our result (6.57 ± 0.08 keV).

PG 1244+026.— The best-fit line center energy is $6.13^{+0.12}_{-0.10}$ keV in our analysis. Jiménez-Bailón et al. (2005) and Porquet et al. (2004) obtained the line center energy at $6.65^{+0.07}_{-0.18}$ keV and $6.66^{+0.09}_{-0.07}$ keV, respectively.

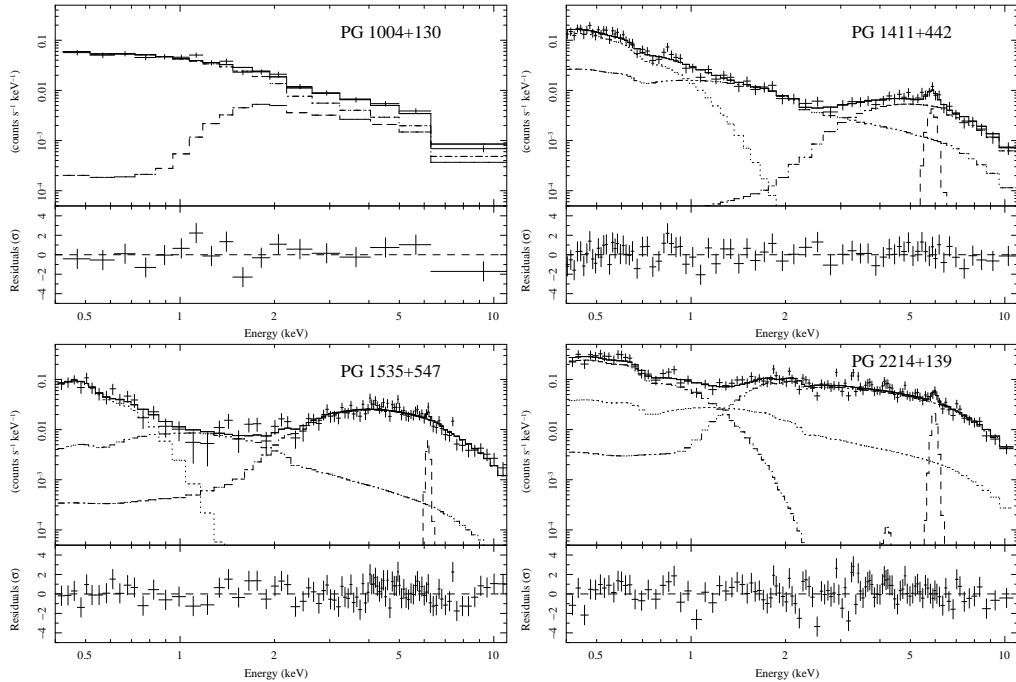


FIG. 8.— Spectra of highly absorbed quasars.

TABLE 6
SPECTRAL PARAMETERS FOR QUASARS NEWLY ANALYZED IN THIS PAPER

PG	Γ	kT (keV)	$(N_{\text{H}})_{z=0}^{\text{a}}$ (10^{22} cm^{-2})	Edge/ τ (keV)	E_{Fe} (keV)	σ (keV)	EW (eV)	$\chi^2/\text{d.o.f.}$
1302-102	$1.66^{+0.10}_{-0.11}$	$0.20^{+0.02}_{-0.04}$	$0.00^{+0.06}_{-0.00}$	—	—	—	—	64/63
1448+273	$2.25^{+0.11}_{-0.11}$	$0.12^{+0.01}_{-0.02}$	$0.05^{+0.01}_{-0.01}$	$0.66^{+0.02}_{-0.01}/0.27^{+0.07}_{-0.07}$	$6.41^{+0.54}_{-0.24}$	0.1f	93^{+142}_{-93}	260/290
			$0.23^{+0.06}_{-0.14}$					
2130+099	$1.65^{+0.03}_{-0.02}$	$0.11^{+0.00}_{-0.00}$	$0.05^{+0.01}_{-0.01}$	$0.72^{+0.02}_{-0.01}/0.29^{+0.06}_{-0.07}$	$6.45^{+0.07}_{-0.12}$	$0.02^{+0.22}_{-0.02}$	139^{+495}_{-139}	182/139
2233+134	$2.17^{+0.19}_{-0.17}$	$0.19^{+0.03}_{-0.03}$	$0.05^{+0.03}_{-0.03}$	$0.89^{+0.03}_{-0.04}/0.63^{+0.25}_{-0.23}$	—	—	—	117/96
.

NOTE. — PG 1448+273 requires two blackbody components to represent soft excess.

^a Foreground absorption within our Galaxy

TABLE 7
SPECTRAL PARAMETERS FOR QUASARS REANALYZED IN THIS PAPER.

PG	Γ	kT (keV)	$(N_{\text{H}})_{z=0}^{\text{a}}$ (10^{22} cm^{-2})	Edge/ τ (keV)	E_{Fe} (keV)	σ (keV)	EW (eV)	$\chi^2/\text{d.o.f.}$
0003+199	$2.25^{+0.01}_{-0.01}$	$0.13^{+0.00}_{-0.00}$	$0.03^{+0.00}_{-0.00}$	$0.65^{+0.01}_{-0.01}/0.16^{+0.02}_{-0.02}$	$6.60^{+0.13}_{-0.02}$	$0.35^{+0.16}_{-0.09}$	192^{+134}_{-97}	626/483
0804+761	$2.30^{+0.09}_{-0.09}$	—	$0.02^{+0.01}_{-0.01}$	—	$6.57^{+0.08}_{-0.08}$	0.1f	1406^{+2195}_{-1353}	141/138
1244+026	$2.54^{+0.01}_{-0.01}$	$0.15^{+0.01}_{-0.01}$	$0.01^{+0.01}_{-0.01}$	—	$6.13^{+0.12}_{-0.10}$	0.1f	642^{+1031}_{-642}	197/187
1613+658	$1.92^{+0.10}_{-0.10}$	$0.13^{+0.02}_{-0.03}$	$0.04^{+0.02}_{-0.02}$	$0.73^{+0.16}_{-0.07}/0.22^{+0.19}_{-0.20}$	—	—	—	109/97

^a Foreground absorption within our Galaxy

PG 1613+658.— A line feature is not clearly seen at ~ 6.4 keV in our spectrum. No detection is consistent with the result of Page et al. (2004a) (EW < 85 eV), while Page et al. (2004b) reported EW = 96 ± 59 eV.

REFERENCES

Ashton, C. E., Page, M. J., Blustin, A. J., Puchnarewicz, E. M., Branduardi-Raymont, G., Mason, K. O., C  rdova, F. A., & Priedhorsky, W. C. 2004, MNRAS, 355, 73
Ballantyne, D. R., Ross, R. R., & Fabian, A. C. 2001, MNRAS, 327, 10
Boroson, T. A., & Green, R. F. 1992, ApJS, 80, 109
Brandt, W. N., Laor, A., & Wills, B. J. 2000, ApJ, 528, 637
Brinkmann, W., Grupe, D., Branduardi-Raymont, G., & Ferrero, E. 2003, A&A, 398, 81

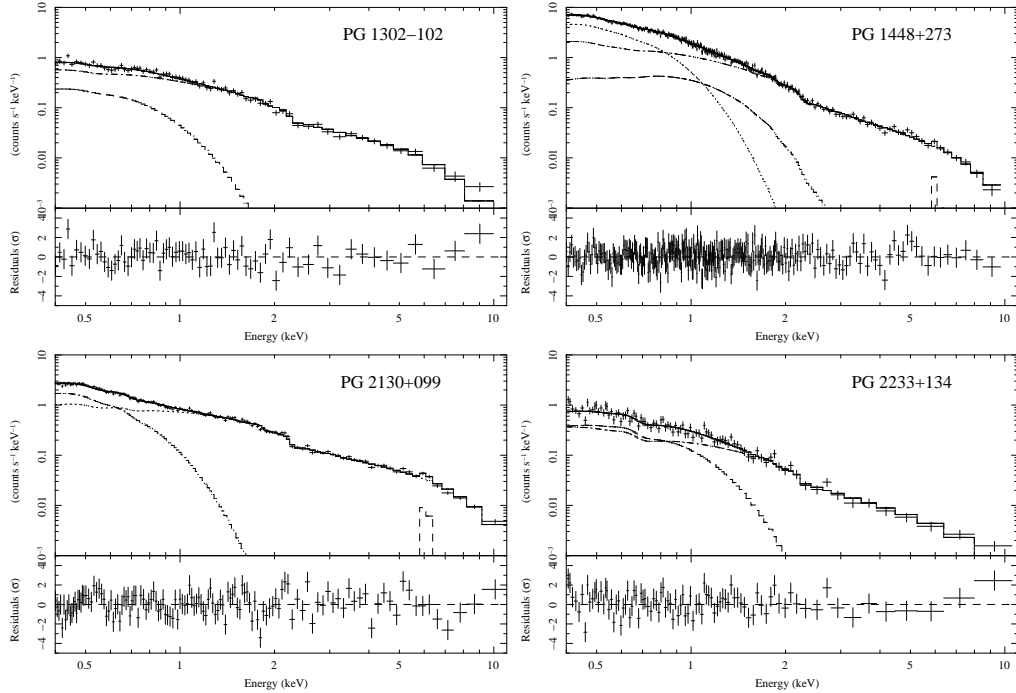


FIG. 9.— Spectra of PG quasars newly analyzed in this paper.

Brinkmann, W., Papadakis, I. E., & Ferrero E. 2004, *A&A*, 414, 107
 Brinkmann, W., Wang, T., Grupe, D., & Raeth, C. 2006 *A&A*, 450, 925
 Brocksopp, C., Starling, R. L. C., Schady, P., Mason, K. O., Romero-Colmenero, E., & Puchnarewicz, E. M. 2006, *MNRAS*, 366, 953
 Brusa, M., Gilli, R., & Comastri, A. 2005, *ApJ*, 621, L5
 Comastri, A., Brusa, M., & Gilli, R. 2007, in *Relativistic Astrophysics and Cosmology — Einstein's Legacy*, ed. B. Aschenbach et al. (astro-ph/0603139)
 Crummy, J., Fabian, A. C., Brandt, W. N., & Boller, Th. 2005, *MNRAS*, 361, 1197
 Crummy, J., Fabian, A. C., Gallo, L., & Ross, R. R. 2006, *MNRAS*, 365, 1067
 Dasgupta, S., Rao, A. R., Dewangan, G. C., & Agrawal, V. K. 2005, *ApJ*, 618, 87
 Dickey, J. M., & Lockman, F. J. 1990, *ARA&A*, 28, 215
 Fabian, A. C., Rees, M. J., Stella, L., & White, N. E. 1989, *MNRAS*, 238, 729
 George, I. M., Turner, T. J., Netzer, H., Nandra, K., Mushotzky, R. F., & Yaqoob, T. 1998, *ApJS*, 114, 73
 George, I. M., Turner, T. J., Yaqoob, T., Netzer, H., Laor, A., Mushotzky, R. F., Nandra, K., & Takahashi, T. 2000, *ApJ*, 531, 52
 Gondoin, P., Orr, A., Lumb, D., & Santos-Lleó, M. 2002, *A&A*, 388, 74
 Iwasawa, K., & Taniguchi, Y. 1993, *ApJ*, 413, 15
 Jiménez-Bailón, E., Piconcelli, E., Guainazzi, M., Schartel, N., Rodríguez-Pascual, P. M., & Santos-Lleó, M. 2005, *A&A*, 435, 449
 Lehmann, I., et al. 2001, *A&A*, 371, 833
 Mainieri, V., Bergeron, J., Hasinger, G., Lehmann, I., Rosati, P., Schmidt, M., Szokoly, G., & Della Ceca, R. 2002, *A&A*, 393, 425
 Mateos, S., Barcons, X., Carrera, F. J., Ceballos, M. T., Hasinger, G., Lehmann, I., Fabian, A. C., & Streblyanska, A. 2005, *A&A*, 444, 79
 Matt, G., Fabian, A. C., & Ross, R. R. 1993, *MNRAS*, 262, 179
 Miller, B. P., Brandt, W. N., Gallagher, S. C., Laor, A., Wills, B. J., Garmire, G. P., & Schneider, D. P. 2006, *ApJ*, 52, 163
 Miniutti, G., & Fabian, A. C. 2006, *MNRAS*, 366, 115
 Nandra, K., George, I. M., Mushotzky, R. F., Turner, T. J., & Yaqoob, T. 1997a, *ApJ*, 477, 602
 — 1997b, *ApJ*, 488, L91
 Nayakshin, S., Kazanas, D., & Kallman, T. R. 2000, *ApJ*, 537, 833
 Page, K. L., O'Brien, P. T., Reeves, J. N., & Turner, M. J. L. 2004a, *MNRAS*, 347, 316
 Page, K. L., Schartel, N., Turner, M. J. L., & O'Brien, P. T. 2004b, *MNRAS*, 352, 523
 Piconcelli, E., Jiménez-Bailón, E., Guainazzi, M., Schartel, N., Rodríguez-Pascual, P. M., & Santos-Lleó, M. 2005, *A&A*, 432, 15
 Porquet, D., Reeves, J. N., O'Brien, P., & Brinkmann, W. 2004, *A&A*, 422, 85
 Pounds, K. A., Reeves, J. N., King, A. R., Page, K. L., O'Brien, P. T., & Turner, M. J. L. 2003, *MNRAS*, 345, 705
 Pounds, K. A., King, A. R., Page, K. L., & O'Brien, P. T. 2003, *MNRAS*, 346, 1025
 Pounds, K. A., & Page, K. L. 2006, *MNRAS*, 372, 1275
 Reeves, J. N., Porquet, D., & Turner, T. J. 2004, *ApJ*, 615, 150
 Reynolds, C. S., & Nowak, M. A. 2003, *Phys. Rep.*, 377, 389
 Ross, R. R., & Fabian, A. C. 1999, *MNRAS*, 261, 74
 Schartel, N., Rodríguez-Pascual, P. M., Santos-Lleó, M., Clavel, J., Guainazzi, M., Jiménez-Bailón, E., & Piconcelli, E. 2005, *A&A*, 433, 455
 Schmidt, M., et al. 1998, *A&A*, 329, 495
 Schmidt, M., & Green, R. F. 1983, *ApJ*, 269, 352
 Streblyanska, A., Hasinger, G., Finoguenov, A., Barcons, X., Mateos, S., & Fabian, A. C. 2005, *A&A* 432, 395
 Tanaka, Y., et al. 1995, *Nature*, 375, 659
 Weymann, R. J., Morris, S. L., Foltz, C. B., & Hewett, P. C. 1991, *ApJ*, 373, 23
 Yaqoob, T. 2005, in *Populations of High Energy Sources in Galaxies*, ed. M. J. A. Meurs & G. Fabbiano (Cambridge: Cambridge Univ. Press), 461
 Yaqoob, T., & Padmanabhan, U. 2004, *ApJ*, 604, 63
 Yuan, W., Siebert, J., & Brinkmann, W. 1998, *A&A*, 334, 498
 Życki, P. T., & Czerny, B. 1994, *MNRAS*, 266, 653
 Życki, P. T., Krolik, J. H., Zdziarski, A. A., & Kallman, T. R. 1994, *ApJ*, 437, 597